Optimal Integrated Inner Controller Design in AC Microgrids

Yazdan Batmani, Yousef Khayat, Shahabeddin Najafi, and Josep M. Guerrero, *Fellow, IEEE*

***Abstract*—The optimal design of a microgrid's primary control's inner loops is a severe challenge in high-bandwidth (BW) applications. Mostly, nonoptimal controllers are given as a sublevel design for the current and voltage inner loops. Unlike conventional methods, such as proportional resonant, proportional-integral, and finite-set model predictive control, in this article, an optimal integrated inner controller is proposed based on a linear quadratic tracking (LQT) methodology. In the proposed method, a model-based optimal LQT controls the microgrid's voltage and current simultaneously. By employing this method, a performance index, which is a system energy indicator is minimized, and the BW of the controller is systematically adjusted through the employed weighting matrices in the performance index. Besides, a current limiting mechanism is provided for the proposed method, which discriminates its applicability for practical purposes. Unlike the conventional current limiting algorithms, which limit the sine-waveform of the current, the proposed method limits the amplitude of the current and causes less current and voltage distortions during over-current situations. The simulation and experimental results reveal the superiority of the proposed method.**

***Index Terms*—Inner controller, microgrid (MG), optimal tracking, primary control (PC).**

NOMENCLATURE

BW	Bandwidth.
DGU	Distributed generation unit.
ESSs	Energy storage systems.
FS-MPC	Finite set model predictive control.
LQG	Linear quadratic Gaussian.
LQE	Linear quadratic estimation.
LQR	Linear quadratic regulator.
LQT	Linear quadratic tracking.
LTR	Loop transfer recovery.
MG	Microgrid.
PC	Primary control.
PCC	Point of common coupling.
PI	Proportional integral.
PR	Proportional resonant.
RES	Renewable energy source.
THD	Total harmonic distortion.
VSC	Voltage source converter.

VARIABLES:

$\mathbf{A}$	State space matrix of the actual system for a DGU.
$\mathbf{B}$	Input matrix of the actual system for a DGU.
$\mathbf{C}$	Output matrix of the actual system for a DGU.
$\mathbf{A}_{\text{des}}$	State space matrix of the desired system for a DGU.
$\mathbf{C}_{\text{des}}$	Output matrix of the desired system for a DGU.
$\tilde{\mathbf{A}}$	State space matrix of the augmented system for a DGU.
$\tilde{\mathbf{B}}$	Input matrix of the augmented system for a DGU.
$\mathbf{Q}$	Quality of response weighting matrix for the LQT design.
$\tilde{\mathbf{Q}}$	Quality of response weighting matrix of the augmented system.
$\mathbf{R}$	Control effort weighting matrix for the LQT design.
$\mathbf{K}_{\text{f}}$	State feedback gain matrix.
$\mathbf{K}_{\text{ff}}$	Feed-forward gain matrix.
γ	Discount factor.
$v_{\text{s}}(t)$	Inverter output voltage.
$v_{\text{c}}(t)$	Filter capacitor voltage.
$v_{\text{t}}(t)$	DGU output voltage.
$i_{\text{f}}(t)$	Current of the input inductance of the LCL filter.
$i_{\text{c}}(t)$	Current of the output inductance of the LCL filter.
R_f	Resistance of the input inductance in the LCL filter.
R_c	Resistance of the output inductance in the LCL filter.
L_f	Input inductance of the LCL filter.
C_{f}	Capacitance of the LCL filter.
L_c	Output inductance of the LCL filter.
ω	Angular frequency.
σ	System eigenvalues.
$\mathbb{R}$	Set of real numbers.
$\mathbb{R}^n$	Euclidean space of all n-dimensional real vectors.
$\mathbb{R}^{n\times m}$	Space of all $n \times m$ real matrices.
$\frac{\text{d}}{\text{d}t}(.)$	Derivation with respect to time.
$\exp(.)$	Exponential function.
$\mathbf{I}_n$	$n \times n$ identity matrix.
$\mathbf{diag}(x)$	Diagonal matrix with the elements of the vector x.

Manuscript received February 1, 2022; accepted March 27, 2022. Date of publication April 6, 2022; date of current version May 23, 2022. This work was supported by the Department of Energy Technology, Aalborg University under the Villum Investigator Grant 25920 as a part of the Villum Investigator Program CROM funded by the Villum Foundation. Recommended for publication by Associate Editor I. Slama-Belkhodja. *(Corresponding author: Yazdan Batmani.)*

Yazdan Batmani, Yousef Khayat, and Shahabeddin Najafi are with Smart/Micro Grids Research Center, Department of Electrical Engineering, University of Kurdistan, Sanandaj 6617715175, Iran (e-mail: y.batmani@uok.ac.ir; y.khayat@uok.ac.ir; shahabedin.najafi@uok.ac.ir).

Josep M. Guerrero is with the Department of Energy Technology, Aalborg University, DK 9220 Aalborg, Denmark (e-mail: joz@energy.aau.dk).

Color versions of one or more figures in this article are available at https://doi.org/10.1109/TPEL.2022.3165355.

Digital Object Identifier 10.1109/TPEL.2022.3165355

I. Introduction

MG IS an essential concept, which has recently emerged to integrate DGUs and ESSs for feeding loads either in the grid-connected or islanded modes of operation [1]. In MGs, power electronic VSCs are mostly used for conversing RESs' energy. To attain a secure and reliable operation of MGs, hierarchical control architectures have been introduced in three main control layers: PC layer, secondary control layer, and tertiary control layer [2]–[4].

The PC layer is a decentralized layer, typically consisting of dual cascaded inner loops of the current and voltage controllers, and droop mechanisms [5]–[7]. Stabilization of the frequency and voltage amplitudes of each DGU as well as appropriate power sharing among DGUs are the main control duties of the PC layer. While stabilization of the frequency and voltage amplitudes is generally achieved by a dual current and voltage control loops, the power sharing is achieved by the droop mechanism [8], [9].

Voltage and current loops, mostly introduced by the dual inner loops, are traditionally realized by the PI and PR controllers [10]–[12]. For a safe operation of power VSCs, a current saturation block is necessary, which is placed to limit the generated reference current by the voltage loop. By this way, the employed VSC keeps a safe operation even for overloads and faulty conditions [13]. A more detailed study that covers the modeling, analysis, and design in the stationary frame of the PR-based inner loops for the paralleled VSCs in the MGs has been provided in [14]. For the same aims, a detailed small-signal modeling and stability analysis of the MGs in the synchronous frame for the PI-based inner loops has been recently given in [15] and [16].

In recent years, high-performance controllers and strategies have been proposed to deal with the control objectives in the inner loop layers, such that not only are the voltage and frequency stabilized, but they can also limit the over-currents concerns. In this regard, in [17]–[19], the MPC-based solutions have been designed to satisfy the PC objectives. A full state-variable direct MPC, which presents a simple structure, has been introduced in [20]. Unlike the conventional cascaded control loops, this solution tracks the generated reference set-points in one single loop. However, it suffers from distortions and harmonics issues of the current and voltage waveforms of the current limiter during overloads and faulty conditions. In these situations, the MPC-based solutions limit the sine-waveform; and consequently, more distortions in the current and voltage waveforms are appeared.

Using robust controllers to synthesis multiobjective optimal controllers has become a popular tool in recent advanced control designs. Employing robust approaches, such as H_2, H_∞, mixed H_2/H_∞, and iterative μ-based solution for the PC layer design has been already considered in [21]–[24]. Despite their robust performances, the current limitation, as a safe operation requirement of the VSCs, has not been satisfied. In this way, in [25], a robust sliding mode and a mixed H_2/H_∞ output feedback PC have been designed for the AC MGs, where a droop controller, a mixed H_2/H_∞ voltage controller, and an adaptive back-stepping current controller have been allocated in a cascade structure. The performance of the controller under overload conditions,

To improve the transient behavior in both the islanded and grid-connected modes, developing the PC based on the state feedback strategy is becoming popular in the recent works. Pérez-Ibacache *et al.* [26] have proposed a controller by considering a dynamic output feedback control problem solved using an LQG-LTR procedure. This solution, however, requires solving the LQE and LQR problems, where its adjustment needs to follow a heuristic approach. In addition, the LQG-LTR procedure only unravels the separate minimization of the LQE and LQR problems, and as checked in [26]–[28], may significantly reduce the performance of the closed-loop system. The drawback associated with limiting the current during overloads for a safe operation of the VSCs is still remained for the LQR-based optimal reference tracking proposed in [29].

Modifying the inner controller structure such that the controller BW is systematically adjusted by tuning the design parameters is a practical requirement [30], [31]. Indeed, if the primary controller BW can be increased in the hierarchical structure, the outer control layers can also be established with higher BW controllers; and thus, it leads to a faster response in high BW applications [32]. In the primary controller's traditional structures, the voltage and current control loops are constructed in cascade. Moreover, every outer loop is designed to have a slower response or a smaller BW than the inner control loops. Consequently, the overall controller has a slow dynamic performance. This matter causes some additional constraints on designing the hierarchical controller's outer layers (i.e., the secondary and tertiary) [33], [34]. Therefore, increasing the BW of the inner loops is a practical way to cope with this problem.

In this article, instead of the traditional dual inner loops based on the voltage and current controllers, an LQT controller is developed with the following contributions.

1) The proposed integrated optimal LQT controller satisfies the inner loop control requirements in both the grid connected and islanded operation modes of the VSCs in an MG. By employing the proposed scheme, not only are the voltage and current stability for the DGUs guaranteed through an optimal state feedback control law, but the converter can also keep its safe operation during overloads, voltage sags, and fault conditions due to its novel adaptive current limitation mechanism.
2) Using the proposed method, the feedback and feedforward gains are computed by specifying two weighting matrices. In addition, the BW of the controller can be systematically adjusted through the employed weighting matrices in the design procedure, which makes the proposed solution more applicable in high BW applications.
3) More importantly, unlike the mentioned LQR-based optimal reference tracking control strategies in the literature, such as [29], the proposed method is equipped with a current limitation strategy, which is capable to tackle the overloads and faults properly. Besides, while the current limiting algorithm employed in the FS-MPC limits the sine-waveform of the current, and consequently, leads to more distortion in the voltage and current waveforms during limiting [19], the proposed method limits the amplitude of the current and causes less current and voltage

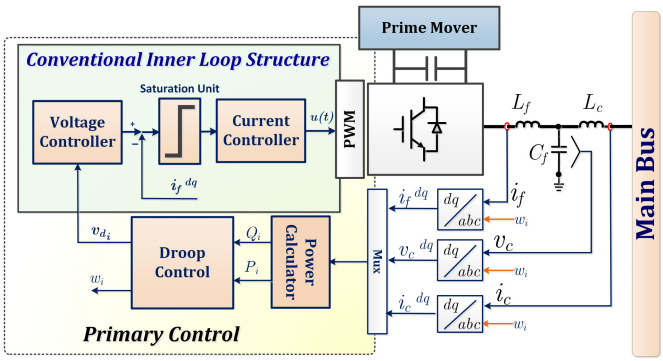

Fig. 1. Block diagram of a DGU including the physical layer and the primary control structure.

distortions. These findings are comprehensively shown through simulation and experimental results, and also, in a quantitative analysis on the THD percentage during overloads and voltage sags.

4) The proposed optimal inner loop control scheme is designed in an offline mode just through finding a gain matrix by solving an algebraic Riccati equation, where there is no need to a continuous data processing with a high sampling time.
5) The proposed method leads to a second-order inner controller; it increases the six-order open-loop system to an eight-order closed-loop system. Therefore, the order of the closed-loop system is not increased considerably. While for the conventional PI and PR methods, the closed-loop degree of the inner-loops leads to a system with higher order of ten.

The rest of this article is organized as follows. In Section II, a mathematical model of the VSC-based DGUs is obtained. In Section III, the design procedure of the LQT is presented. The optimal integrated inner controller, designed based on the LQT method, is reviewed in Section IV. In Section V, the simulation and the experimental results of applying the proposed technique to an example MG are represented. Finally, Section VI concludes this article.

II. Mathematical Modeling of DGs

Fig. 1 shows the block diagram of a DGU in an autonomous MG, where the architecture of the PC and the conventional dual inner loops are illustrated. The nonlinear behavior of each DGU can be formulated in its own dq reference frame, where it is assumed that the reference frame of the ith DGU is rotating by the frequency of ω_i. The power calculator and droop controller blocks, shown in Fig. 1, compute the active and reactive powers and provide the voltage and frequency references for the voltage controller, as well as the operating frequency for the inverter bridge by using the following droop mechanism:

$$\begin{aligned} \omega_i &= \omega^* - m_{p_i} P_i \\ v_{d_i} &= V_n - n_{Q_i} Q_i \end{aligned} \tag{1}$$

where v_{d_i} is the reference value for the output voltage magnitude provided for the inner voltage controller; ω_i is for the angular frequency of the DGU; P_i and Q_i are the filtered active and reactive power measured at the DGU's terminal, respectively; m_{p_i} and n_{Q_i} are the droop coefficients; ω^* and V_n are the control references of the droop control mechanism. The droop coefficients are selected based on the active and reactive power ratings of each DGU. In addition, to extract the fundamental components of the calculated active and reactive powers P_i and Q_i, low-pass filters with the cut-off frequency ω_{c_i} are used. The dynamics of the power calculator can be written as [35]

$$\begin{aligned} \dot{P}_i &= -w_{c_i} P_i + w_{c_i}(v_{cd} i_{cd} + v_{cq} i_{cq}) \\ \dot{Q}_i &= -w_{c_i} Q_i + w_{c_i}(v_{cq} i_{cd} - v_{cd} i_{cq}) \end{aligned} \tag{2}$$

where v_{cd}, v_{cq}, i_{cd}, and i_{cq} are the direct and quadrature components of v_c and i_c in Fig. 1. The dynamics of the voltage and current inner loops can be found in [35]–[37]. The dynamics of the DGUs' LC filter and output line connector in the dq frame can also be acquired as follows:

$$\begin{aligned} \frac{\mathrm{d}}{\mathrm{d}t} i_{\mathrm{fd}}(t) &= \omega_i i_{\mathrm{fq}}(t) + \frac{1}{L_{\mathrm{f}}} v_{\mathrm{sd}}(t) - \frac{1}{L_{\mathrm{f}}} v_{\mathrm{cd}}(t) - \frac{R_{\mathrm{f}}}{L_{\mathrm{f}}} i_{\mathrm{fd}}(t) \\ \frac{\mathrm{d}}{\mathrm{d}t} i_{\mathrm{fq}}(t) &= -\omega_i i_{\mathrm{fd}}(t) + \frac{1}{L_{\mathrm{f}}} v_{\mathrm{sq}}(t) - \frac{1}{L_{\mathrm{f}}} v_{\mathrm{cq}}(t) - \frac{R_{\mathrm{f}}}{L_{\mathrm{f}}} i_{\mathrm{fq}}(t) \\ \frac{\mathrm{d}}{\mathrm{d}t} v_{\mathrm{cd}}(t) &= \omega_i v_{\mathrm{cq}}(t) + \frac{1}{C_{\mathrm{f}}} i_{\mathrm{fd}}(t) - \frac{1}{C_{\mathrm{f}}} i_{\mathrm{cd}}(t) \\ \frac{\mathrm{d}}{\mathrm{d}t} v_{\mathrm{cq}}(t) &= -\omega_i v_{\mathrm{cd}}(t) + \frac{1}{C_{\mathrm{f}}} i_{\mathrm{fq}}(t) - \frac{1}{C_{\mathrm{f}}} i_{\mathrm{cq}}(t) \\ \frac{\mathrm{d}}{\mathrm{d}t} i_{\mathrm{cd}}(t) &= \omega_i i_{\mathrm{cq}}(t) - \frac{R_{\mathrm{c}}}{L_{\mathrm{c}}} i_{\mathrm{cd}}(t) + \frac{1}{L_{\mathrm{c}}} v_{\mathrm{cd}}(t) - \frac{1}{L_{\mathrm{c}}} v_{\mathrm{td}}(t) \\ \frac{\mathrm{d}}{\mathrm{d}t} i_{\mathrm{cq}}(t) &= -\omega_i i_{\mathrm{cd}}(t) - \frac{R_{\mathrm{c}}}{L_{\mathrm{c}}} i_{\mathrm{cq}}(t) + \frac{1}{L_{\mathrm{c}}} v_{\mathrm{cq}}(t) - \frac{1}{L_{\mathrm{c}}} v_{\mathrm{tq}}(t). \end{aligned} \tag{3}$$

By defining the state vector $x(t) = [i_{\mathrm{fd}}(t) \;\; i_{\mathrm{fq}}(t) \;\; v_{\mathrm{cd}}(t) \;\; v_{\mathrm{cq}}(t) \;\; i_{\mathrm{cd}}(t) \;\; i_{\mathrm{cq}}(t)]^{\mathrm{T}}$, the input vector $u(t) = [v_{\mathrm{sd}}(t) \; v_{\mathrm{sq}}(t)]^{\mathrm{T}}$, and the output vector $y(t) = [v_{\mathrm{cd}}(t) \;\; v_{\mathrm{cq}}(t)]^{\mathrm{T}}$, the following state-space representation is obtained:

$$\begin{aligned} \frac{\mathrm{d}}{\mathrm{d}t} x(t) &= \mathbf{A}x(t) + \mathbf{B}u(t) + \mathbf{d}v_{\mathrm{t_{dq}}}(t) \\ y(t) &= \mathbf{C}x(t) \end{aligned} \tag{4}$$

where $\mathbf{A} \in \mathbb{R}^{6\times 6}$, $\mathbf{B} \in \mathbb{R}^{6\times 2}$, $\mathbf{d} \in \mathbb{R}^{6\times 2}$, and $\mathbf{C} \in \mathbb{R}^{2\times 6}$ are as follows:

$$\mathbf{A} = \begin{bmatrix} \frac{-R_{\mathrm{f}}}{L_{\mathrm{f}}} & \omega_i & \frac{-1}{L_{\mathrm{f}}} & 0 & 0 & 0 \\ -\omega_i & \frac{-R_{\mathrm{f}}}{L_{\mathrm{f}}} & 0 & \frac{-1}{L_{\mathrm{f}}} & 0 & 0 \\ \frac{1}{C_{\mathrm{f}}} & 0 & 0 & \omega_i & \frac{-1}{C_{\mathrm{f}}} & 0 \\ 0 & \frac{1}{C_{\mathrm{f}}} & -\omega_i & 0 & 0 & \frac{-1}{C_{\mathrm{f}}} \\ 0 & 0 & \frac{1}{L_{\mathrm{c}}} & 0 & \frac{-R_{\mathrm{c}}}{L_{\mathrm{c}}} & \omega_i \\ 0 & 0 & 0 & \frac{1}{L_{\mathrm{c}}} & -\omega_i & \frac{-R_{\mathrm{c}}}{L_{\mathrm{c}}} \end{bmatrix}$$

$$\mathbf{B}=\begin{bmatrix}\frac{1}{L_{\rm f}} & 0 & 0 & 0 & 0 & 0\\ 0 & \frac{1}{L_{\rm f}} & 0 & 0 & 0 & 0\end{bmatrix}^{\rm T}$$

$$\mathbf{d}=\begin{bmatrix}0 & 0 & 0 & 0 & \frac{-1}{L_{\rm c}} & 0\\ 0 & 0 & 0 & 0 & 0 & \frac{-1}{L_{\rm c}}\end{bmatrix}^{\rm T}$$

$$\mathbf{C}=\begin{bmatrix}0 & 0 & 1 & 0 & 0 & 0\\ 0 & 0 & 0 & 1 & 0 & 0\end{bmatrix}.$$

III. Linear Quadratic Tracker

Consider the following linear continuous-time system:

$$\frac{\rm d}{{\rm d}t}x(t)=\mathbf{A}x(t)+\mathbf{B}u(t),\ \ x(0)=x_0$$
$$y(t)=\mathbf{C}x(t) \tag{5}$$

where $x(t)\in\mathbb{R}^n$, $u(t)\in\mathbb{R}^m$, $y(t)\in\mathbb{R}^q$, and x_0 are the state vector, control input, system output, and initial condition, respectively; $\mathbf{A}\in\mathbb{R}^{n\times n}$, $\mathbf{B}\in\mathbb{R}^{n\times m}$, and $\mathbf{C}\in\mathbb{R}^{q\times n}$ are three constant matrices. The goal of the optimal tracking problem is to obtain $u(t)$ such that $y(t)$ tracks the reference signal $y_{\rm des}(t)\in\mathbb{R}^q$ and the following performance index is minimized while all the system states stay bounded:

$$J=\int_0^\infty \exp(-\gamma t)\left(e^{\rm T}(t)\mathbf{Q}e(t)+u^{\rm T}(t)\mathbf{R}u(t)\right){\rm d}t \tag{6}$$

where $e(t)=y(t)-y_{\rm des}(t)$ is the tracking error; $\mathbf{Q}\in\mathbb{R}^{q\times q}$ and $\mathbf{R}\in\mathbb{R}^{m\times m}$ are positive semidefinite and positive definite weighting matrices, respectively; $\gamma>0$ is called the discount factor. In the cost function (6), $e^{\rm T}(t)\mathbf{Q}e(t)$ is the error's energy, and $u^{\rm T}(t)\mathbf{R}u(t)$ is the energy consumed by the controller. $\mathbf{Q}$ and $\mathbf{R}$ are used to make a tradeoff between these two terms. For example, increasing $\mathbf{Q}$ leads to a faster closed-loop system with larger control efforts. Presume that the desired reference signal is the output of the following system:

$$\frac{\rm d}{{\rm d}t}x_{\rm des}(t)=\mathbf{A}_{\rm des}x_{\rm des}(t),\ \ x_{\rm des}(0)=x_{\rm d0}$$
$$y_{\rm des}(t)=\mathbf{C}_{\rm des}x_{\rm des}(t) \tag{7}$$

where $x_{\rm des}(t)\in\mathbb{R}^{n_{\rm des}}$ and $x_{\rm d0}$ are the state and initial condition of the generator system of the desired reference signal, respectively; $\mathbf{A}_{\rm des}\in\mathbb{R}^{n_{\rm des}\times n_{\rm des}}$ and $\mathbf{C}_{\rm des}\in\mathbb{R}^{q\times n_{\rm des}}$ are two constant matrices, which are determined based on the desired reference signal.

By defining $X(t)=\exp(-\gamma t)[x(t)\ \ x_{\rm des}(t)]^{\rm T}\in\mathbb{R}^{n+n_{\rm des}}$, and $U(t)=\exp(-\gamma t)u(t)\in\mathbb{R}^m$, the dynamics of $X(t)$ can be determined as follows:

$$\frac{\rm d}{{\rm d}t}X(t)=\tilde{\mathbf{A}}X(t)+\tilde{\mathbf{B}}U(t) \tag{8}$$

where

$$\tilde{\mathbf{A}}=-\gamma\mathbf{I}_{n+n_{\rm des}}+\begin{bmatrix}\mathbf{A} & \mathbf{0}_{n\times n_{\rm des}}\\ \mathbf{0}_{n_{\rm des}\times n} & \mathbf{A}_{\rm des}\end{bmatrix},\tilde{\mathbf{B}}=\begin{bmatrix}\mathbf{B}\\ \mathbf{0}_{n_{\rm des}\times m}\end{bmatrix}. \tag{9}$$

According to the new variables $X(t)$ and the new control input $U(t)$, (6) can be rewritten as follows [38]:

$$J=\int_0^\infty X^{\rm T}(t)\tilde{\mathbf{Q}}X(t)+U^{\rm T}(t)\mathbf{R}U(t){\rm d}t \tag{10}$$

where $\tilde{\mathbf{Q}}=[\mathbf{C}\ \ -\mathbf{C}_{\rm des}]^{\rm T}\mathbf{Q}[\mathbf{C}\ \ -\mathbf{C}_{\rm des}]$ is a positive semidefinite matrix [38]. Since the optimal control problem defined by (8) and (10) has the same equations with a standard LQR problem, the following optimal control law is achieved [38]:

$$U(t)=-\mathbf{R}^{-1}\tilde{\mathbf{B}}^{\rm T}\mathbf{P}X(t) \tag{11}$$

where $\mathbf{P}\in\mathbb{R}^{(n+n_{\rm des})\times(n+n_{\rm des})}$ is the unique symmetric positive definite solution of the following algebraic Riccati equation:

$$\tilde{\mathbf{A}}^{\rm T}\mathbf{P}+\mathbf{P}\tilde{\mathbf{A}}-\mathbf{P}\tilde{\mathbf{B}}\mathbf{R}^{-1}\tilde{\mathbf{B}}^{\rm T}\mathbf{P}+\tilde{\mathbf{Q}}=\mathbf{0}. \tag{12}$$

Equation (12) has a unique symmetric positive definite solution if and only if the pair $(\tilde{\mathbf{A}},\tilde{\mathbf{B}})$ is stabilizable and $\tilde{\mathbf{Q}}$ is positive semidefinite [39]. Regarding (11) and based on the definitions of $X(t)$ and $U(t)$, the optimal solution of the original tracking problem, defined by (5) and (6), is determined as follows [38]:

$$u(t)=-\mathbf{R}^{-1}\tilde{\mathbf{B}}^{\rm T}\mathbf{P}[x^{\rm T}(t)\ \ x_{\rm des}^{\rm T}(t)]^{\rm T}. \tag{13}$$

The determined control law is a function of the states of the main system (5) and the reference signal generator (7). In this way, (13) can be rewritten as follows:

$$u(t)=-\mathbf{K}_{\rm f}x(t)-\mathbf{K}_{\rm ff}x_{\rm des}(t) \tag{14}$$

where the feedback and feed-forward gains $\mathbf{K}_{\rm f}\in\mathbb{R}^n$ and $\mathbf{K}_{\rm ff}\in\mathbb{R}^{n_{\rm des}}$ are obtained from (13), simultaneously.

Fig. 2 shows the design procedure of the optimal tracking controller. For more details, readers can refer to [38].

IV. Proposed Optimal Integrated Control

In this section, as depicted in Fig. 3, an optimal LQT controller is designed for a DGU to track the voltage reference generated in the droop control sublevel. The proposed controller is also equipped with a current limiter mechanism to satisfy the current limiting requirements, as an important feature for power converter VSCs.

A. LQT Controller Design

Step 1: The optimal control problem, defined by (5) and (6), needs to select appropriate weighting matrices $\mathbf{Q}$ and $\mathbf{R}$. The

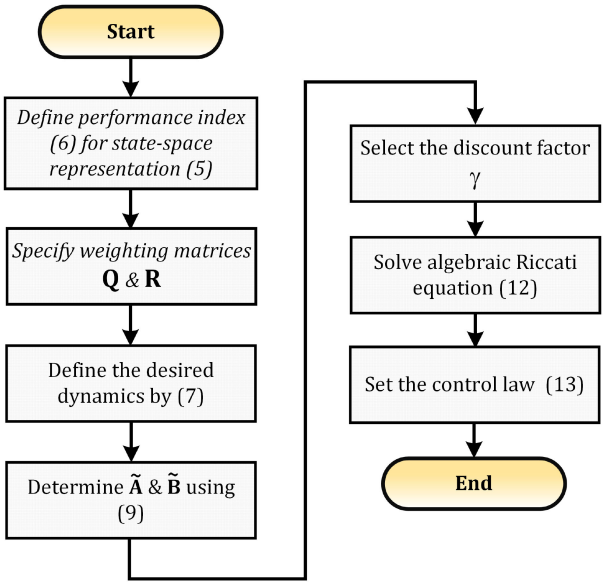

Fig. 2. Flowchart of the LQT controller design.

Bryson's method can be used to choose these weighting matrices as $\mathbf{Q} = \mathbf{diag}(q_1, \ldots, q_{\rm n})$ and $\mathbf{R} = \mathbf{diag}(r_1, \ldots, r_{\rm m})$ with [40]

$$q_i = \frac{1}{\text{maximum acceptable value of } x_i^2(t)}$$

$$r_i = \frac{1}{\text{maximum acceptable value of } u_i^2(t)} \tag{15}$$

where $x_i(t)$ is the ith state variable of the system, and $u_i(t)$ is the ith control input. The maximum value of $x_i(t)$ and $u_i(t)$ are the physical constraints on their amplitudes that are imposed to the design procedure. Besides, the Bryson's method is a rule of thumb, and the designer can systematically change the values of these elements to achieve the desired objectives. These weighting matrices present two degrees of freedom in the proposed design technique. As mentioned earlier, adjusting the controller's BW is one of the significant merits of the proposed method. Hence, the designer can benefit from the freedom to modulate the controller's BW. For instance, the BW of the controller can be widened (the controller's response can be accelerated) by increasing the system state weighting matrix, although at the expense of an increased control effort.

Step 2: Since the reference signals $v_{\rm cd,ref}(t)$ and $v_{\rm cq,ref}(t)$ are constant, their time derivatives are zero. By defining $x_{\rm des}(t) = [v_{\rm cd,ref}(t) \;\; v_{\rm cq,ref}(t)]^{\rm T}$, the following equations are utilized for the desired reference signal:

$$\begin{aligned} \frac{\rm d}{{\rm d}t} x_{\rm des}(t) &= \mathbf{0}_{2\times 2} x_{\rm des}(t) = \mathbf{A}_{\rm des} x_{\rm des}(t) \\ y_{\rm des}(t) &= \mathbf{I}_2 x_{\rm des}(t) = \mathbf{C}_{\rm des} x_{\rm des}(t). \end{aligned} \tag{16}$$

Step 3: Due to (4), (8), and (16), $\tilde{\mathbf{B}}$ and $\tilde{\mathbf{A}}$ are determined as follows:

$$\tilde{\mathbf{B}} = \begin{bmatrix} \frac{1}{L_{\rm f}} & 0 & 0 & 0 & 0 & 0 & 0 & 0 \\ 0 & \frac{1}{L_{\rm f}} & 0 & 0 & 0 & 0 & 0 & 0 \end{bmatrix}^{\rm T} \tag{17}$$

$$\tilde{\mathbf{A}} = \begin{bmatrix} -\alpha & \omega & -\frac{1}{L_{\rm f}} & 0 & 0 & 0 & 0 & 0 \\ -\omega & -\alpha & 0 & -\frac{1}{L_{\rm f}} & 0 & 0 & 0 & 0 \\ \frac{1}{C_{\rm f}} & 0 & -\gamma & \omega & -\frac{1}{C_{\rm f}} & 0 & 0 & 0 \\ 0 & \frac{1}{C_{\rm f}} & -\omega & -\gamma & 0 & -\frac{1}{C_{\rm f}} & 0 & 0 \\ 0 & 0 & \frac{1}{L_{\rm c}} & 0 & -\beta & \omega & 0 & 0 \\ 0 & 0 & 0 & \frac{1}{L_{\rm c}} & -\omega & -\beta & 0 & 0 \\ 0 & 0 & 0 & 0 & 0 & 0 & -\gamma & 0 \\ 0 & 0 & 0 & 0 & 0 & 0 & 0 & -\gamma \end{bmatrix}$$

where $\alpha = \gamma + R_{\rm f}/L_{\rm f}$ and $\beta = \gamma + R_{\rm c}/L_{\rm c}$.

Step 4: The rank of the controllability matrix of $(\tilde{\mathbf{A}}, \tilde{\mathbf{B}})$ is six; and therefore, $(\tilde{\mathbf{A}}, \tilde{\mathbf{B}})$ is uncontrollable where both the uncontrollable modes belong to (16). However, the stabilizability of $(\tilde{\mathbf{A}}, \tilde{\mathbf{B}})$ is the necessary condition for having a unique positive solution of (12). The eigenvalues of the uncontrollable modes are $-\gamma$ that are negative for any $\gamma > 0$; and hence, these modes are stabilizable, and (12) has a unique symmetric positive definite solution.

Step 5: The optimal control law is obtained as follows:

$$\begin{aligned} u(t) = \begin{bmatrix} v_{\rm sd}(t) \\ v_{\rm sq}(t) \end{bmatrix} &= -\mathbf{K}_{\rm ff} \begin{bmatrix} \hat{v}_{\rm cd,ref}(t) & \hat{v}_{\rm cq,ref}(t) \end{bmatrix}^{\rm T} \\ &\quad - \mathbf{K}_{\rm f} \begin{bmatrix} i_{\rm fd}(t) & i_{\rm fq}(t) & v_{\rm cd}(t) & v_{\rm cq}(t) & i_{\rm cd}(t) & i_{\rm cq}(t) \end{bmatrix}^{\rm T} \end{aligned} \tag{18}$$

where $\hat{v}_{\rm cd,ref}(t)$ and $\hat{v}_{\rm cq,ref}(t)$ are the reference signals determined by the current limiter block (see Section IV-B). Fig. 3 shows how the proposed control law can be employed as an optimal inner loop control by multiplying the calculated gains $\mathbf{K}_{\rm f}$ and $\mathbf{K}_{\rm ff}$ into the state variables of the MG and desired reference signal, respectively.

Remark 1: Paying attention to (17), in the presence of the proposed LQT inner controller, the order of the closed-loop system is increased from six to eight. The conventional PI controllers, however, increase the system order from six to ten.

Remark 2: To eliminate harmonics and to reduce the negative-sequence of current of the proposed method, one can inspire from [41] for extending harmonic-based LQT inner loops and rejecting the other harmonic orders, by repeating the design procedure for other harmonics.

B. Current Restriction

One of the vital protection aspects for DGUs is keeping the converter's safety during overloads and in faulty conditions. This

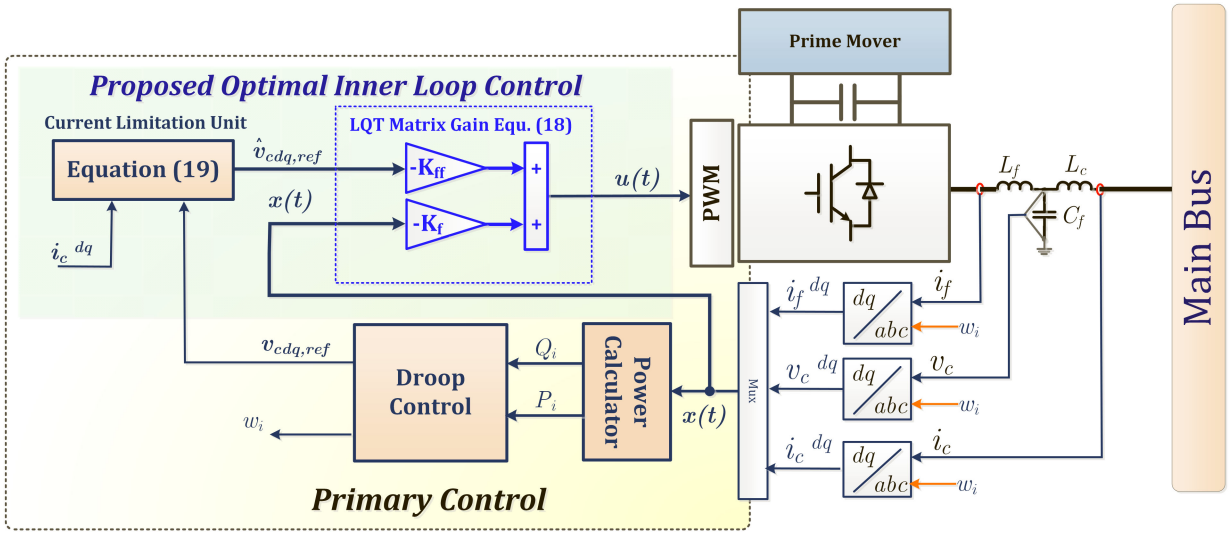

Fig. 3. Proposed optimal LQT inner controller scheme.

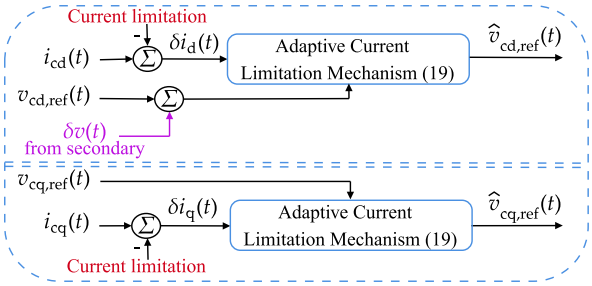

Fig. 4. Proposed mechanism for a safe limitation of the converter's current.

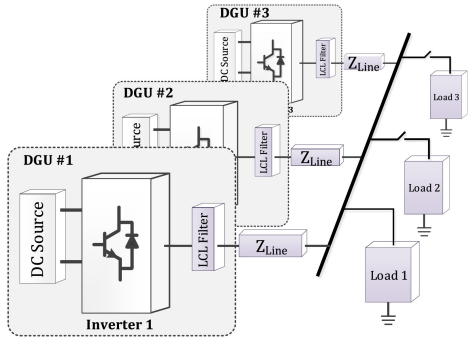

Fig. 5. Diagram of the considered MG with three DGUs.

function is conventionally realized through limiters in the PI or PR controllers; however, for recent controllers it is still remained as a concern. In the traditional inner controls, the saturation blocks are generally used after generating the reference current by the voltage loop controller, as shown earlier in Fig. 1. In the proposed method, nevertheless, to achieve this important protection requirement, as shown in Fig. 2, a current limiter mechanism is considered. The structure of this current limiter is shown in Fig. 4. When the output current reaches its thresholds, the reference voltage generated by (16) is automatically changed by an adaptive scheme. In this way, the current is not allowed to violate from its constraint. This adaptive mechanism uses the following laws:

$$\hat{v}_{\mathrm{cd,ref}}(t) = \begin{cases} v_{\mathrm{cd,ref}}(t), & \delta i_{\mathrm{d}}(t) \le -0.2; \\ v_{\mathrm{cd,ref}}(t) - \zeta_{\mathrm{d}}(t), & \delta i_{\mathrm{d}}(t) > -0.2; \end{cases}$$

$$\hat{v}_{\mathrm{cq,ref}}(t) = \begin{cases} v_{\mathrm{cq,ref}}(t), & \delta i_{\mathrm{q}}(t) \le -0.2; \\ v_{\mathrm{cq,ref}}(t) - \zeta_{\mathrm{q}}(t), & \delta i_{\mathrm{q}}(t) > -0.2; \end{cases}$$

$$\zeta_{\mathrm{d}}(t) = \exp\left(\frac{1}{\ln(v_{\mathrm{cd,ref}}(t)) - \delta i_{\mathrm{d}}(t)}\right)$$

$$\zeta_{\mathrm{q}}(t) = \exp\left(\frac{1}{\ln(v_{\mathrm{cq,ref}}(t)) - \delta i_{\mathrm{q}}(t)}\right). \quad (19)$$

As can be seen from (19), the inputs of the current limiter mechanism are the voltage reference signals ($v_{\mathrm{cd,ref}}(t)$ and $v_{\mathrm{cq,ref}}(t)$), which are provided by the droop controller. Its outputs are the reference signals $\hat{v}_{\mathrm{cd,ref}}(t)$ and $\hat{v}_{\mathrm{cq,ref}}(t)$, which are applied to the designed LQT controller. The outputs and inputs of this current restriction mechanism are the same until $i_{\mathrm{cd}}(t)$ and $i_{\mathrm{cq}}(t)$ approach their restriction bounds. In other words, if $\delta i_{\mathrm{d}}(t) \le -0.2$ ($\delta i_{\mathrm{q}}(t) \le -0.2$), $\hat{v}_{\mathrm{cd,ref}}(t)$ ($\hat{v}_{\mathrm{cq,ref}}(t)$) is exactly equal to $v_{\mathrm{cd,ref}}(t)$ ($v_{\mathrm{cq,ref}}(t)$). Nevertheless, if $\delta i_{\mathrm{d}}(t) > -0.2$ ($\delta i_{\mathrm{q}}(t) > -0.2$), which means they are close to their limitation bounds, $v_{\mathrm{cd,ref}}(t)$ ($v_{\mathrm{cq,ref}}(t)$)) is changed by $\zeta_{\mathrm{d}}(t)$ ($\zeta_{\mathrm{q}}(t)$).

V. Simulation and Experimental Results

In this section, to evaluate the performance of the proposed optimal integrated inner controller, an MG consists of three DGUs (see Fig. 5) is considered. Some scenarios are studied, and the achieved results of both simulation and laboratory tests are compared. In the simulation and laboratory tests, the DGUs' utilized parameters are reported in Table I. By solving the algebraic Riccati equation (12), the feedback and feedforward

TABLE I
ELECTRICAL AND CONTROL PARAMETERS

Electrical Parameters		
Parameter	**Symbol**	**Value**
DC source voltage	V_{DC}	650 V
Nominal voltage magnitude	V_{MG}	325 V
Nominal frequency	f	50 Hz
Switching frequency	f_s	10 kHz
Capacitance of LCL filter	C_f	25 μF
Input inductance of LCL filter	L_f	1.8 mH
Output inductance of LCL filter	L_c	1.8 mH
Output and filter resistances	R_c, R_f	0.1 Ω
Line impedance 1	Z_{Line}	0.8 Ω , 3.6 mH
Load 1, 3	Z_1	43 Ω , 0.3 H
Load 2	Z_2	124 Ω , 0.1 H

Control Parameters				
		Parameter	**Symbol**	**Value**
Droop Layer		*P-w* droop coefficient	m	0.002 W/rad
		Q-v droop coefficient	n	0.02 VAr/V
Inner Loop	Traditional *PR*	Current proportional term	k_{ip}	0.5
		Current resonance term	k_{ir}	1000
		Voltage proportional term	k_{vp}	0.05
		Voltage resonance term	k_{vr}	120
	Proposed LQT	Error weighting matrix	$\mathbf{Q}$	$10^7\mathbf{I}_2$
		Error weighting matrix	$\mathbf{R}$	$\mathbf{I}_2$
		Discount factor	γ	10^{-5}

gains are computed as follows:

$$\mathbf{K}_{\mathrm{f}} = 10^3 \begin{bmatrix} 1.9 & 0 & 3.2 & 0 & -1.9 & 0 \\ 0 & 1.9 & 0 & 3.2 & 0 & -1.9 \end{bmatrix}$$

$$\mathbf{K}_{\mathrm{ff}} = 10^3 \begin{bmatrix} -3.2 & 0.0018 \\ -0.0018 & 3.2 \end{bmatrix}. \quad (20)$$

A. Stability Analysis

To evaluate the robustness and stability of the proposed LQT inner loop controller, a set of analysis is done, which is also compared with the conventional dual inner loops based on the PR controller. To investigate the system stability and its robustness against output impedance uncertainties for both the LQT and conventional PR controllers, sensitivity analyses on the closed-loop system are done. Fig. 6 shows the eigenvalues traces for different output filter inductances, such that the 3-D presentations show detailed changes of the eigenvalues near the imaginary axis. As can be observed from Fig. 6(a), the possible range to avoid the passivity and resonance concerns for the conventional PR is determined based on the right half-plane eigenvalues; where the eigenvalue trace shows that the PR-based inner loop instability for the output filter inductance is more than 2.33 mH. However, the LQT controller shows a more robust behavior, such that for the output filter inductance near 5 mH, the system still keeps its stability.

Besides the stated robustness features of the proposed method, its superiority for increasing the controller's BW is revealed in Fig. 7, where the Bode magnitude plots of both the conventional PR-based and the LQT controllers are shown. From this figure, one can see that the BW in the proposed method is approximately 12.5 times more than the conventional method,

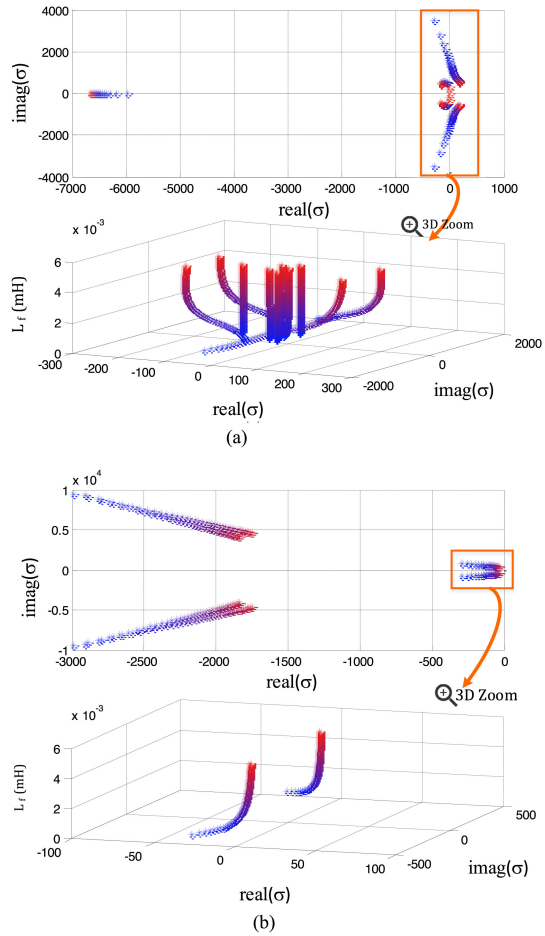

Fig. 6. Eigenvalues sensitivity analysis for variations in the output filter's inductance, when it changes from 0.1 mH (in blue color) to 5 mH (in red color). (a) The conventional PR-based dual inner loops. (b) The optimal LQT.

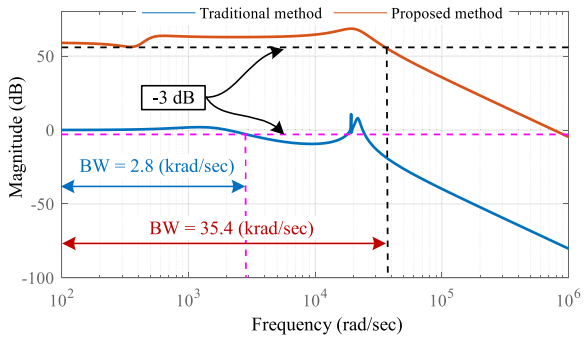

Fig. 7. Bode magnitude plots of the proposed and traditional controllers.

which shows its applicability in high BW applications. The transfer function of the system under the proposed LQT controller is $\tilde{\mathbf{C}}(s\mathbf{I}_8 - \mathbf{A}_{\mathrm{cl}})^{-1}\tilde{\mathbf{B}}$, where $\tilde{\mathbf{C}} = [\mathbf{C} \quad \mathbf{0}_{2\times 2}]$ and $\mathbf{A}_{\mathrm{cl}} = \tilde{\mathbf{A}} - \tilde{\mathbf{B}}[\mathbf{K}_{\mathrm{f}}^{\mathrm{T}} \quad \mathbf{K}_{\mathrm{ff}}^{\mathrm{T}}]^{\mathrm{T}}$.

B. Simulation Results

Scenario I. Load change: A common load change and a comparison with the conventional dual inner loop based on the PR controller are considered in this scenario. The load increases

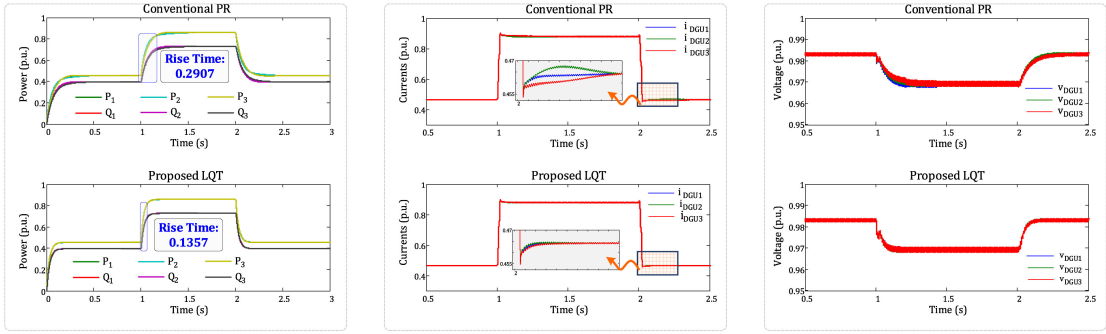

Fig. 8. Comparison between the PR controller (top plots) and the proposed LQT controller (bottom plots) for the load change. (a) Active and reactive power sharings. (b) RMS current waveforms. (c) RMS voltage waveforms.

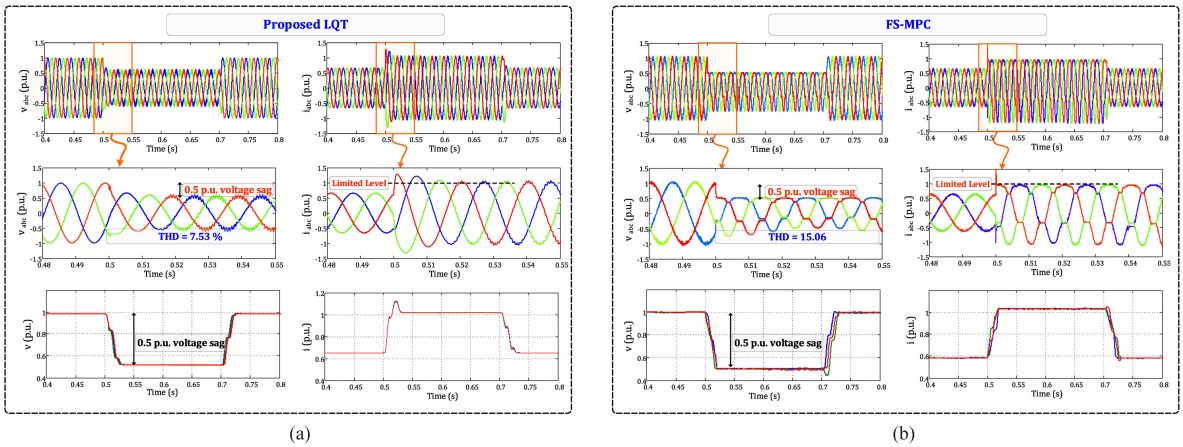

Fig. 9. Comparison of the current limiting capability between the LQT and FS-MPC techniques. (a) Voltage waveforms in the *abc* frame (top-left), current waveforms in the *abc* frame (top-right), their zooms in illustration as well as the RMS values for the LQT controller. (b) Voltage waveforms in the *abc* frame (top-left), current waveforms in the *abc* frame (top-right), their zooms in illustration (middle) as well as the RMS values (bottom) for the FS-MPC.

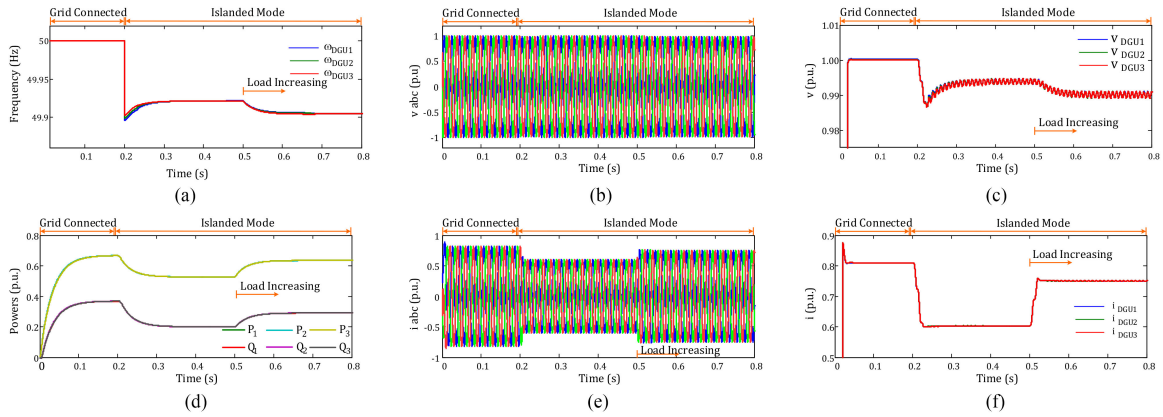

Fig. 10. Performance assessment for transition from the grid connected to the islanded mode of operation using the proposed LQT-based inner loop. (a) MG frequency. (b) The *abc* frame voltage waveforms of DGU 1 in pu. (c) RMS values of the voltage of all the DGUs. (d) Active and reactive powers in pu. (e) The *abc* frame current waveforms of DGU 1 in pu. (f) RMS values of the current of all the DGUs.

at $t = 1$ s, and it reduces at $t = 2$ s. Fig. 8(a) shows the active and reactive power sharings for the studied MG. In comparison with the PR controller, the LQT provides a better dynamic for passing the transients after the load changes. The same superiority can be observed from Fig. 8(b) and (c), where the RMS current and RMS voltage of DGUs are depicted, respectively. In order to indicate some quantitative analysis, the closed-loop transfer functions from the reference voltage to the output voltage for the controllers are calculated. The rise time and settling time of the PR controller are 0.2907 and 0.4371 s, respectively (see

TABLE II
THD COMPARISON FOR DIFFERENT VOLTAGE SAG LEVELS DURING OVERLOAD CONDITIONS

Voltage Sag (VS)	0.0 % VS	10 % VS	20 % VS	50 % VS
Conventional PR	2.53	7.74	11.05	21.22
FS-MPC	1.73 %	5.96 %	9.91 %	15.06 %
Proposed LQT	1.64 %	2.18 %	5.48 %	7.53 %

Fig. 8). While these indices for the LQT are 0.1357 and 0.1904 s, respectively; and therefore, the proposed LQT outperforms the conventional PR controller.

Scenario II. Current saturation capability: As mentioned earlier, one of the main important features which an inner controller must have is its ability to limit the converter current for a safe operation. As shown in Fig. 9(a), the designed controller properly limits the over-current. At $t=0.5$ s, after a load increasing, the output current is limited to 1 pu; however, the load increasing causes a considerable voltage drop. The same waveforms can be achieved even for short circuit faults, where the voltage is reduced more, while the current is still limited to 1 pu. The same scenario is implemented while the inner loop controller is incorporated by an FS-MPC for a comparison, as shown in Fig. 9(b). The load is increased at $t=0.5$ s and decreased again at $t=0.7$ s, and the current is limited by the employed constrained in the FS-MPC's objective function, as formulated and described in [19]. The most important difference between these two controllers for the current limiting is concealed in their limitation procedures. In the FS-MPC, the current limitation is imposed on the sinusoidal waveforms, such that the FS-MPC cuts the over-current after generating the sinusoidal waveforms, which leads to a considerable distortion in the current sinusoidal waveform; and consequently, the voltage waveforms are distorted as well. While in the proposed method, the limitation is imposed on the amplitude; and then, the sinusoidal waveforms are generated. This leads to less distortion in the current and voltage waveforms, as can be observed from the zoomed subplots in Fig. 9(a) and (b). Table II shows a quantitative comparison among the conventional PR, FS-MPC, and LQT as inner loops, when there are different voltage sags and the converter has to supply 15% overload. The LQT has the lowest output-voltage THD under a wide range of voltage sags. The output-voltage THD of the LQT controller indicates that it has the least sensitivity (i.e., stronger robustness) to voltage sags during the overload conditions.

Scenario III. MG Mode Transition: In this scenario, the performance of the proposed method is investigated by considering a smooth transient during mode changes from the grid-connected to the islanded mode of operation. As shown in all the subplots of Fig. 10, the MG operates in the grid-connected mode over the time interval $t\in[0\,0.2]$ s and intentionally disconnects from the grid at $t=0.2$ s. For $t\in[0\,0.2]$ s, the voltage and frequency of the MG are fixed by the grid (since the MG is operated by the grid-connected mode), as shown in Fig. 10(a) and (c), respectively. Meanwhile, there are active and reactive power injections toward the main grid for $t\in[0\,0.2]$ s, as shown in Fig. 10(d) and can also be inferred from the current waveforms in Fig. 10(e) and (f). After disconnecting from the main grid

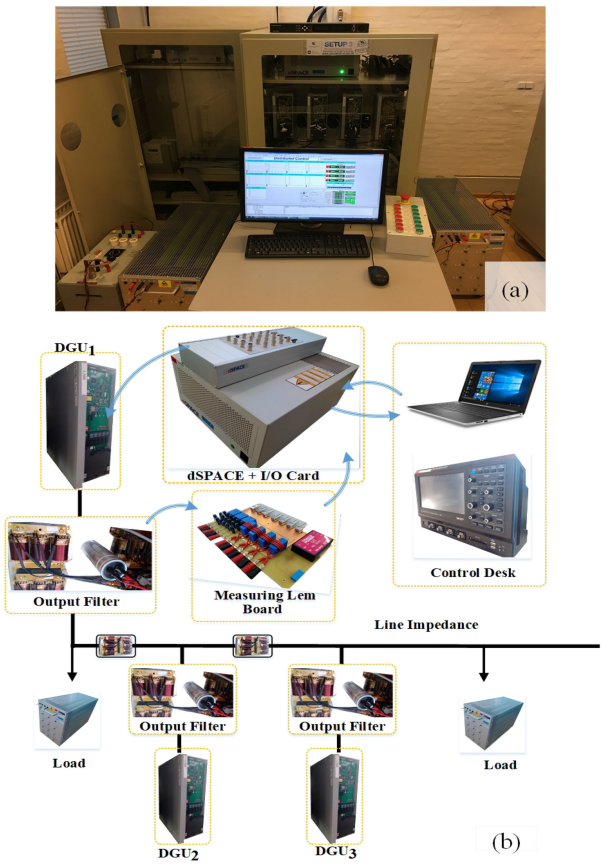

Fig. 11. Laboratory environment and setup circuit diagram. (a) Control desk. (b) Circuit diagram of the experimental setup.

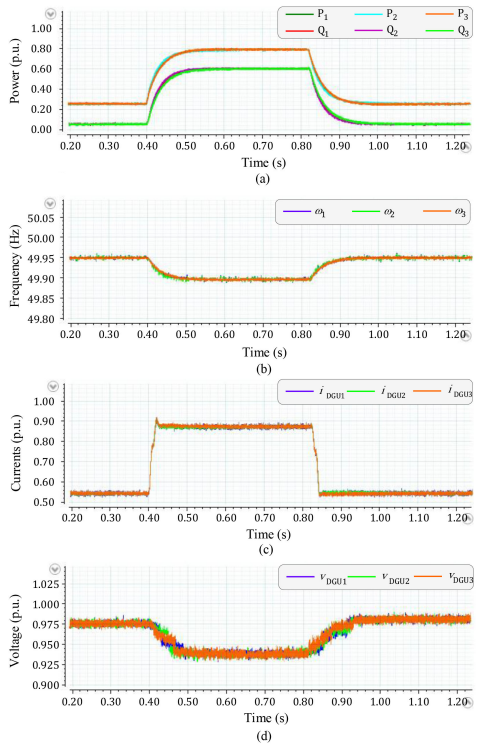

Fig. 12. Experimental results for evaluating a load change performance. (a) Active and reactive powers of all the DGUs. (b) Frequency waveforms. (c) RMS current values of all the DGUs. (d) RMS voltage values of all the DGUs.

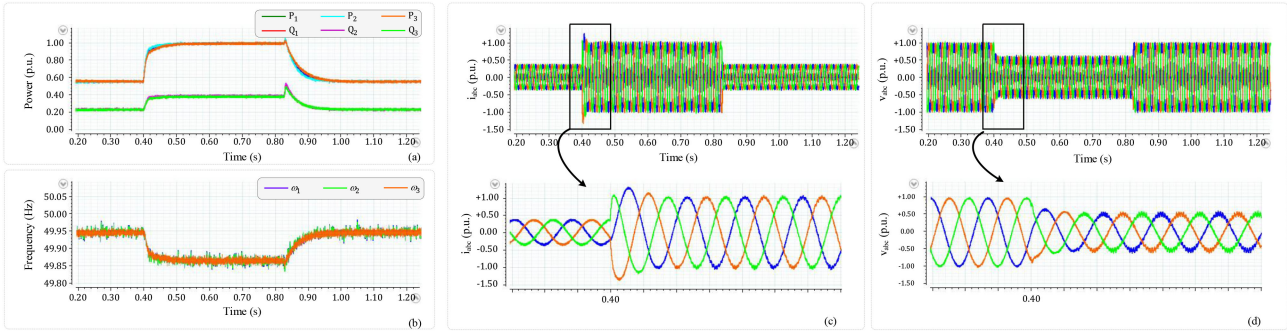

Fig. 13. Experimental results for evaluating the current limiting capability during overload conditions. (a) Active and reactive powers of all the DGUs. (b) Frequency waveforms. (c) Current waveforms of DGU_1 in the *abc* fram and its zoom-in illustration. (d) Voltage waveforms of DGU_1 in the *abc* fram and its zoom-in illustration.

at $t = 0.2$ s, the system is governed by the droop controller and only feeds the MG loads. In addition, the voltage and frequency stability are still kept by the LQT, which these can be inferred even after a load change over $t \in [0.2\, 0.8]$ s. During the islanding mode, i.e., $t \in [0.6\, 0.8]$ s, the frequency and voltage are governed by the droop layer; and thus, the frequency and RMS voltages are reduced from the nominal values to the generated set-points by the droop layer, as shown in Fig. 10(a) and (c), respectively. In addition to active and reactive power waveforms shown in Fig. 10(d), the performance of the LQT, can be seen from the *abc* frame voltage waveforms of the DGU 1, the RMS voltage of all the DGUs, the *abc* frame current waveforms of the DGU 1, and the RMS current of all the DGUs shown in Fig. 10(b), (c), (e), and (f), correspondingly. The performance of the proposed inner loop shows a smooth transition from the grid-connected to the islanded mode of operation, even for load changes at $t = 0.5$ s after disconnecting form the grid.

C. Experimental Results

Experiments are performed on a lab-scale MG, as shown in Fig. 11, which includes three 2.2 kVA droop-based VSCs. The VSCs are supplied by a Regatron dc power source and convert the dc power into a symmetric three-phase ac voltage. The power conversion is realized by coding the proposed method on a DS 1006 dSPACE control interface to generate a 10 kHz switching frequency for triggering the VSC's IGBTs, while the VCSs use the LCL filters to reduce the switching harmonics and notches. To model the line impedance, which connects the units, series RL circuits are employed. All the electrical and control parameters of the system are listed in Table I.

Scenario I. Load Change: This case proposes the experimented results dealing with a load change, shown in Fig. 12. The active and reactive power sharings among all the DGUs, frequency, RMS values of the current and voltage of all the DGUs are shown in Fig. 12(a)–(d), correspondingly. At the beginning, a resistive load is connected as a common load, and 0.2 pu of its active power are fed by each unit, where the frequency and voltages are around 49.95 Hz and 0.975 pu, respectively. Then, after a load increasing at $t = 0.4$ s, each DGU supplies $0.8 + j0.6$ pu active and reactive powers, and the power is still properly shared among the units. The frequency of the units is stabilized around 49.9 Hz, and the voltage of units are dropped around 0.925 pu. Fig. 12 shows that the proposed LQT-based method successfully keeps the stability of the MG, and the power sharing is remained properly during load changes.

Scenario II. Current Restricting: The ability of the LQT controller to restrict the converter currents during overload situations is experimented in this scenario. The power sharing and frequency waveforms of all the units are shown in Fig. 13(a) and (b), respectively. The *abc* frame voltage and current waveforms of the first DGU are presented in Fig. 13(c) and (d), respectively. During the overload or faulty conditions, the voltage can drop based on the severity of the fault or the amount of the overload. According to Fig. 13, the output current is correctly limited to 1.0 pu by increasing a common load, and the voltage is dropped around 0.6 pu.

VI. Conclusion

Unlike conventional dual inner loops for the VSCs in an MG, this article proposed an optimal LQT, which satisfied inner loop control requirements of the VSCs to operate safety in both the grid-connected and islanded modes. Traditionally, the inner controller of the VSCs has a cascade structure consists of a voltage controller and a current controller; where usually, a PI or PR controller is designed for them. In addition to low BW challenges of the conventional controllers, parameter tuning of these controllers makes it difficult to achieve the desired performance. In this article, to attain the optimal performance and establish a systematic design of an inner loop controller, an integrated structure was proposed based on the LQT method. In comparison with the conventional PI and PR solutions, the controller's high BW feature discriminates the proposed solution in high BW applications. Moreover, its simple yet effective current limitation capability provides a safe operation of the VSCs during overloads and in faulty situations. The merits of the proposed method, including its optimality and robust stability, were verified through several simulation and experimental studies.

REFERENCES

[1] N. Hatziargyriou, *Microgrids: Architectures and Control*. Hoboken, NJ, USA: Wiley, 2014.

[2] J. M. Guerrero, J. C. Vasquez, J. Matas, L. G. De Vicuña, and M. Castilla, "Hierarchical control of droop-controlled AC and DC microgrids–A general approach toward standardization," *IEEE Trans. Ind. Electron.*, vol. 58, no. 1, pp. 158–172, Jan. 2011.

[3] J. M. Guerrero, M. Chandorkar, T.-L. Lee, and P. C. Loh, "Advanced control architectures for intelligent microgrids—Part I: Decentralized and hierarchical control," *IEEE Trans. Ind. Electron.*, vol. 60, no. 4, pp. 1254–1262, Apr. 2013.

[4] Y. Khayat *et al.*, "On the secondary control architectures of AC microgrids: An overview," *IEEE Trans. Power Electron.*, vol. 35, no. 6, pp. 6482–6500, Jun. 2020.

[5] Y. Han, P. Shen, X. Zhao, and J. M. Guerrero, "Control strategies for islanded microgrid using enhanced hierarchical control structure with multiple current-loop damping schemes," *IEEE Trans. Smart Grid*, vol. 8, no. 3, pp. 1139–1153, May 2017.

[6] Y. Han, H. Li, P. Shen, E. A. A. Coelho, and J. M. Guerrero, "Review of active and reactive power sharing strategies in hierarchical controlled microgrids," *IEEE Trans. Power Electron.*, vol. 32, no. 3, pp. 2427–2451, Mar. 2017.

[7] C. Dou, Z. Zhang, D. Yue, and Y. Zheng, "MAS-based hierarchical distributed coordinate control strategy of virtual power source voltage in low-voltage microgrid," *IEEE Access*, vol. 5, pp. 11381–11390, 2017.

[8] D. Y. Yamashita, I. Vechiu, and J.-P. Gaubert, "A review of hierarchical control for building microgrids," *Renew. Sustain. Energy Rev.*, vol. 118, 2020, Art. no. 109523.

[9] J. Schiffer, D. Zonetti, R. Ortega, A. M. Stanković, T. Sezi, and J. Raisch, "A survey on modeling of microgrids-from fundamental physics to phasors and voltage sources," *Automatica*, vol. 74, pp. 135–150, 2016.

[10] G. Kyriakarakos, D. D. Piromalis, A. I. Dounis, K. G. Arvanitis, and G. Papadakis, "Intelligent demand side energy management system for autonomous polygeneration microgrids," *Appl. Energy*, vol. 103, pp. 39–51, 2013.

[11] G. Kyriakarakos, D. D. Piromalis, A. I. Dounis, K. G. Arvanitis, and G. Papadakis, "Intelligent demand side energy management system for autonomous polygeneration microgrids," *Appl. Energy*, vol. 103, pp. 39–51, 2013.

[12] T. Vandoorn, J. De Kooning, B. Meersman, and L. Vandevelde, "Review of primary control strategies for islanded microgrids with power-electronic interfaces," *Renew. Sustain. Energy Rev.*, vol. 19, pp. 613–628, 2013.

[13] E. Rokrok, M. Shafie-Khah, and J. P. Catalão, "Review of primary voltage and frequency control methods for inverter-based islanded microgrids with distributed generation," *Renew. Sustain. Energy Rev.*, vol. 82, pp. 3225–3235, 2018.

[14] J. C. Vasquez, J. M. Guerrero, M. Savaghebi, J. Eloy-Garcia, and R. Teodorescu, "Modeling, analysis, and design of stationary-reference-frame droop-controlled parallel three-phase voltage source inverters," *IEEE Trans. Ind. electron.*, vol. 60, no. 4, pp. 1271–1280, Apr. 2013.

[15] M. Naderi, Y. Khayat, Q. Shafiee, T. Dragicevic, H. Bevrani, and F. Blaabjerg, "Interconnected autonomous AC microgrids via back-to-back converters—Part I: Small-signal modeling," *IEEE Trans. Power Electron.*, vol. 35, no. 5, pp. 4728–4740, May 2020.

[16] M. Naderi, Y. Khayat, Q. Shafiee, T. Dragičević, H. Bevrani, and F. Blaabjerg, "Interconnected autonomous AC microgrids via back-to-back converters—Part II: Stability analysis," *IEEE Trans. Power Electron.*, vol. 35, no. 11, pp. 11 801–11 812, Nov. 2020.

[17] A. J. Babqi and A. H. Etemadi, "MPC-based microgrid control with supplementary fault current limitation and smooth transition mechanisms," *IET Gen. Trans. Dist.*, vol. 11, no. 9, pp. 2164–2172, 2017.

[18] Z. Zhang *et al.*, "Advances and opportunities in the model predictive control of microgrids: Part I–Primary layer," *Int. J. Electric. Power Energy Syst.*, vol. 134, 2022, Art. no. 107411.

[19] T. Dragičević, "Model predictive control of power converters for robust and fast operation of AC microgrids," *IEEE Trans. Power Electron.*, vol. 33, no. 7, pp. 6304–6317, Jul. 2018.

[20] Y. Li, Z. Zhang, C. Hu, M. Abdelrahem, R. Kennel, and J. Rodriguez, "A full state-variable direct predictive control for islanded microgrids with parallel converters," *IEEE J. Emerg. Sel. Top. Power Electron.*, vol. 9, no. 4, pp. 4615–4628, Aug. 2021.

[21] H. R. Baghaee, M. Mirsalim, G. B. Gharehpetian, and H. A. Talebi, "A decentralized robust mixed h_2/H_∞ voltage control scheme to improve small/large-signal stability and FRT capability of islanded multi-DER microgrid considering load disturbances," *IEEE Syst. J.*, vol. 12, no. 3, pp. 2610–2621, Sep. 2018.

[22] G. G. Koch, L. A. Maccari, R. C. Oliveira, and V. F. Montagner, "Robust H_∞ state feedback controllers based on linear matrix inequalities applied to grid-connected converters," *IEEE Trans. Ind. Electron.*, vol. 66, no. 8, pp. 6021–6031, Aug. 2019.

[23] M. Armin *et al.*, "Robust extended H_∞ control strategy using linear matrix inequality approach for islanded microgrid," *IEEE Access*, vol. 8, pp. 135883–135896, 2020.

[24] L. Huang, H. Xin, and F. Dörfler, "H_∞-control of grid-connected converters: Design, objectives and decentralized stability certificates," *IEEE Trans. Smart Grid*, vol. 11, no. 5, pp. 3805–3816, Sep. 2020.

[25] M. Raeispour, H. Atrianfar, H. R. Baghaee, and G. B. Gharehpetian, "Robust sliding mode and mixed H_2/H_∞ output feedback primary control of ac microgrids," *IEEE Syst. J.*, vol. 15, no. 2, pp. 2420–2431, Jun. 2021.

[26] R. Pérez-Ibacache, C. A. Silva, and A. Yazdani, "Linear state-feedback primary control for enhanced dynamic response of AC microgrids," *IEEE Trans. Smart Grid*, vol. 10, no. 3, pp. 3149–3161, May 2019.

[27] L. Ravanbod, D. Noll, and P. Apkarian, "An extension of the linear quadratic Gaussian-loop transfer recovery procedure," *IET Control Theory App.*, vol. 6, no. 14, pp. 2269–2278, 2012.

[28] H. Moussa, A. Shahin, J.-P. Martin, S. Pierfederici, and N. Moubayed, "Optimal angle droop for power sharing enhancement with stability improvement in islanded microgrids," *IEEE Trans. Smart Grid*, vol. 9, no. 5, pp. 5014–5026, Sep. 2018.

[29] J. F. Patarroyo-Montenegro, F. Andrade, J. M. Guerrero, and J. C. Vasquez, "A linear quadratic regulator with optimal reference tracking for three-phase inverter-based islanded microgrids," *IEEE Trans. Power Electron.*, vol. 36, no. 6, pp. 7112–7122, Jun. 2021.

[30] R. Heydari, T. Dragicevic, and F. Blaabjerg, "High-bandwidth secondary voltage and frequency control of VSC-based AC microgrid," *IEEE Trans. Power Electron.*, vol. 34, no. 11, pp. 11 320–11 331, Nov. 2019.

[31] R. Heydari *et al.*, "Robust high-rate secondary control of microgrids with mitigation of communication impairments," *IEEE Trans. Power Electron.*, vol. 35, no. 11, pp. 12486–12496, Nov. 2020.

[32] A. R. Jarwar, A. M. Soomro, Z. A. Memon, S. A. Odhano, M. A. Uqaili, and A. S. Larik, "High dynamic performance power quality conditioner for AC microgrids," *IET Power Electron.*, vol. 12, no. 3, pp. 550–556, 2019.

[33] G. Buticchi, L. Costa, and M. Liserre, "Improving system efficiency for the more electric aircraft: A look at dc/dc converters for the avionic onboard dc microgrid," *IEEE Ind. Electron. Mag.*, vol. 11, no. 3, pp. 26–36, Sep. 2017.

[34] J. Yang *et al.*, "Modeling and stability enhancement of a permanent magnet synchronous generator based DC system for more electric aircraft," *IEEE Trans. Ind. Electron.*, vol. 69, no. 3, pp. 2511–2520, Mar. 2022.

[35] A. Bidram, A. Davoudi, F. L. Lewis, and J. M. Guerrero, "Distributed cooperative secondary control of microgrids using feedback linearization," *IEEE Trans. Power Syst.*, vol. 28, no. 3, pp. 3462–3470, Aug. 2013.

[36] A. Bidram, V. Nasirian, A. Davoudi, and F. L. Lewis, *Cooperative Synchronization in Distributed Microgrid Control*. Berlin, Germany: Springer, 2017.

[37] A. Pilloni, A. Pisano, and E. Usai, "Robust finite-time frequency and voltage restoration of inverter-based microgrids via sliding-mode cooperative control," *IEEE Trans. Ind. Electron.*, vol. 65, no. 1, pp. 907–917, Jan. 2018.

[38] H. Modares and F. L. Lewis, "Linear quadratic tracking control of partially-unknown continuous-time systems using reinforcement learning," *IEEE Trans. Automat. Contr.*, vol. 59, no. 11, pp. 3051–3056, Nov. 2014.

[39] F. Lewis and D. Vrabie, *Optimal Control*. Hoboken, NJ, USA: Wiley, 2012.

[40] G. F. Franklin, J. D. Powell, A. Emami-Naeini, and J. D. Powell, *Feedback Control of Dynamic Systems*. Upper Saddle River, NJ, USA: Prentice-Hall, 2002, vol. 4.

[41] M. Savaghebi, A. Jalilian, J. C. Vasquez, and J. M. Guerrero, "Secondary control for voltage quality enhancement in microgrids," *IEEE Trans. Smart Grid*, vol. 3, no. 4, pp. 1893–1902, Dec. 2012.

Yazdan Batmani received the B.Sc. degree in biomedical engineering from the University of Isfahan, Isfahan, Iran, in 2007, and the M.Sc. and Ph.D. degrees in control engineering from K.N. Toosi University of Technology, Tehran, Iran, in 2009 and 2014, respectively.

He is currently an Associate Professor with the Department of Electrical Engineering, University of Kurdistan, Sanandaj, Iran. His research interests include control theory and its applications in biomedical engineering and modern power systems.

Yousef Khayat received the B.Sc. degree in electrical engineering from Urmia University, Urmia, Iran, in 2012, the M.Sc. (Hons.) degree in electrical engineering from the Iran University of Science and Technology, Tehran, Iran, in 2014, and the Ph.D. degree in control of power systems from the University of Kurdistan, Sanandaj, Iran, in 2020.

He was a Visiting Researcher with the Department of Energy, Aalborg University, Aalborg, from October 2018 to February 2020. After that, he was a Research Assistant with the Center for Research on Microgrids (CROM) from March 2019 to March 2020. His research interests include dynamics and control of microgrids, robust, adaptive, and nonlinear control for application of power electronic-based power systems and weak power grids.

Shahabeddin Najafi was born in Kermanshah, Iran, in 1987. He received the B.Sc. degree (Hons.) in electrical engineering and the M.Sc. degree (Hons.) in control engineering from the University of Kurdistan, Sanandaj, Iran, in 2010 and 2018, respectively.

He then joined the Instrumentation and Control (I&C) Group, Operation and Maintenance Corporation, MAPNA Group, Sanandaj, as a Distributed Control System (DCS) Technical Administrator, where he is currently an I&C Expert and a DCS Administrator of the Sanandaj Combined Cycle Power Plant. His research interests include networked control systems, optimal control, and nonlinear control systems.

Josep M. Guerrero (Fellow, IEEE) received the B.S. degree in telecommunications engineering, the M.S. degree in electronics engineering, and the Ph.D. degree in power electronics from the Technical University of Catalonia, Barcelona, Spain, in 1997, 2000, and 2003, respectively.

Since 2011, he has been a Full Professor with the Department of Energy Technology, Aalborg University, Denmark. Since 2014, he has been the Chair Professor with Shandong University, since 2015, he has been a Distinguished Guest Professor with Hunan University and since 2016, he has been a Visiting Professor Fellow with Aston University, U.K., and a Guest Professor with the Nanjing University of Posts and Telecommunications. In 2019, he became a Villum Investigator by The Villum Fonden, which supports the Center for Research on Microgrids (CROM), Aalborg University, where he is the Founder and the Director. He is currently responsible for the Microgrid Research Program with the Department of Energy Technology, Aalborg University, Aalborg, Denmark. He has authored or coauthored more than 600 journal articles in the fields of microgrids and renewable energy systems, which are cited more than 60 000 times. His research interests include different microgrid aspects, including power electronics, distributed energy-storage systems, hierarchical and cooperative control, energy management systems, smart metering and the Internet of Things for ac/dc microgrid clusters, and islanded minigrids; but are especially focused on microgrid technologies applied to offshore wind, maritime microgrids for electrical ships, vessels, ferries, and seaports, and space microgrids applied to nanosatellites and spacecrafts.

Prof. Guerrero was a recipient of the Best Paper Award of the IEEE TRANSACTIONS ON ENERGY CONVERSION for 2014–2015, the Best Paper Prize of IEEE-PES in 2015, and the Best Paper Award of the *Journal of Power Electronics* in 2016. For seven consecutive years, from 2014 to 2020, he was awarded by Clarivate Analytics (former Thomson Reuters) as the Highly Cited Researcher with 50 highly cited papers. He is also an Associate Editor for a number of IEEE publications. He was elevated as an IEEE Fellow in 2015 for his contributions on distributed power systems and microgrids.